Estimating global ocean heat content changes in the upper 1800 m since 1950 and the influence of climatology choice[*]

John M. Lyman[1]

Joint Institute for Marine and Atmospheric Research, University of

Hawaii at Manoa, Honolulu, Hawaii, and NOAA/Pacific Marine

Environmental Laboratory, Seattle, Washington

Gregory C. Johnson

NOAA/Pacific Marine Environmental Laboratory, Seattle, Washington

28 February 2013

[1] *Corresponding author address*: John Lyman, NOAA/Pacific Marine Environmental Laboratory, 7600 Sand Point Way N.E., Bldg. 3, Seattle, Washington 98115-6349, U.S.A.
E-mail: John.Lyman@noaa.gov

14 **Abstract**

15 Ocean heat content anomalies are analyzed from 1950 to 2011 in five distinct depth

16 layers (0–100, 100–300, 300–700, 700–900, and 900–1800 m). These layers correspond

17 to historic increases in common maximum sampling depths of ocean temperature

18 measurements with time, as different instruments—mechanical bathythermograph

19 (MBT), shallow expendable bathythermograph (XBT), deep XBT, early sometimes

20 shallower Argo profiling floats, and recent Argo floats capable of worldwide sampling to

21 2000 m—have come into widespread use. This vertical separation of maps allows

22 computation of annual ocean heat content anomalies and their sampling uncertainties

23 back to 1950 while taking account of in situ sampling advances and changing sampling

24 patterns. The 0–100 m layer is measured over 50% of the globe annually starting in 1956,

25 the 100–300 m layer starting in 1967, the 300–700 m layer starting in 1983, and the

26 deepest two layers considered here starting in 2003 and 2004, during the implementation

27 of Argo. Furthermore, global ocean heat uptake estimates since 1950 depend strongly on

28 assumptions made concerning changes in undersampled or unsampled ocean regions. If

29 unsampled areas are assumed to have zero anomalies and included in the global integrals,

30 the choice of climatological reference from which anomalies are estimated can strongly

31 influence the global integral values and their trend. The sparser the sampling, and the

32 bigger the mean difference between climatological and actual values, the larger the

33 influence.

34

1.   Introduction

35   The world's oceans have absorbed roughly 90% of the anthropogenic warming from

36   greenhouse gasses since the 1960s (Bindoff et al. 2007). This well-documented ocean

37   warming occurs primarily in the upper 0–700 m (Domingues et al. 2008; Ishii and

38   Kimoto 2009; Levitus et al. 2009), but warming has also been observed at intermediate

39   and mid-depths, from 700 to 2000 m (von Schuckmann et al. 2009; Levitus et al. 2012),

40   and in the abyssal ocean, well below 2000 m (Purkey and Johnson 2010; Kouketsu et al.

41   2011).

42   Historically, ocean temperature sampling is inhomogeneous both by geographic

43   region and depth from year to year, with major shifts in observing techniques from

44   decade to decade (Johnson and Wijffels 2011). Accurate but spatially sparse temperature

45   measurements using reversing thermometers, sometimes to full depth, commenced after

46   1874. These thermometers were gradually replaced, starting in the 1960s, with

47   conductivity-temperature-depth (CTD) instruments. Starting in the 1930s, mechanical

48   bathythermographs (MBTs) made it easier to measure the upper ocean temperature

49   (sampling as deep as 145 to 300 m, more often shallower than deeper). They were widely

50   used in the 1950s and 1960s. Starting in 1966, the expendable bathythermograph (XBT)

51   began to replace the MBT for upper ocean thermal sampling, with shallow XBTs

52   (sampling as deep as 460 m) dominant in the 1970s and 1980s, and deep XBTs (sampling

53   as deep as 760 m) dominant in the 1990s. Like MBTs, XBTs are not very accurate

54   (nominally ± 0.1°C for temperature and ± 2% for depth), but both comprise a large part

55   of the observational record of upper ocean temperatures. The profiling CTD floats of the

56   Argo Program (Roemmich et al. 2009) began to provide accurate, year-round sampling of

57   upper ocean temperature starting in 2000. The array started regionally, but became near-

58   global and largely replaced the XBT for distributed ocean measurements by 2005. Early

59   on, some of the floats only sampled to around 1000 m, but as time has gone on, more

60   floats have sampled as deep as the 2000 m Argo target.

61   For climate studies, ocean temperature data are used to estimate ocean heat

62   content anomalies (OHCA). There are many sources of uncertainty in estimates of annual

63   global integrals of OHCA. While reversing thermometers and CTDs are relatively

64   accurate, XBTs have biases in both depth and temperature; different choices of XBT bias

65   corrections lead to large uncertainties from at least 1993 to 2008 (Lyman et al. 2010;

66   Palmer at al. 2010). Mechanical bathythermograph (MBT) bias corrections are equally

67   important in earlier years (Gouretski and Reseghetti 2010; Ishii and Kimoto, 2009).

68   Sampling uncertainty also contributes significantly to the overall uncertainty, and has

69   strong dependence on time (Lyman and Johnson 2008; Domingues et al. 2008; Palmer

70   and Brohan 2011) with larger uncertainties occurring for earlier years when the global

71   ocean is not well sampled. Finally, uncertainties from mapping choices and climatology

72   choice also contribute to the overall uncertainty. Mapping is variously done by bin

73   averaging (Palmer et al. 2007; Gouretski et al. 2012), objective analysis (Ishii and

74   Kimoto, 2009; Levitus et al. 2009), or reduced-space optimal interpolation (Domingues et

75   al. 2008).

76   Climatologies representative of a single era or a long-term mean from which to

77   estimate anomalies in ocean heat content have, historically, been difficult to compute

78   because of sparse historical sampling. Only in recent years has the global ice-free ocean

79   all been sampled adequately in a given year or few years to construct a monthly

80   climatology for a fixed time-period (e.g., Roemmich and Gilson 2009). Having a

81   climatological baseline using data with a well-resolved seasonal cycle for a single, short

82   time period (2005–2010), as is done here, can be very important in improving the

83   accuracy of estimates of global integrals of ocean heat content anomalies in a historically

84   sparsely sampled warming ocean.

85   Here we estimate annual global integrals of ocean heat content in five distinct

86   depth layers from 1950 through 2011. We focus on how sparse irregular sampling and

87   choice of climatological baseline affects estimates of the global integral of OHCA. Here

88   these anomalies are estimated relative to a monthly Argo-period climatology, with a well-

89   resolved seasonal cycle collected over a relatively short time period. The five distinct

90   depth layers (0–100, 100–300, 300–700, 700–900, and 900–1800 m) are chosen to

91   capture the historical sampling patterns of MBTs, XBTs, and Argo floats. Since profiles

92   often terminate at depths slightly shallower than the nominal maximum instrument-

93   sampling depth, layer bottom depths are chosen somewhat shallower than the nominal

94   maximal sampling depths of MBTs (100 vs. 145–300 m), shallow XBTs (300 vs. 460 m),

95   deep XBTs (700 vs. 760 m), and Argo floats (900 and 1800 vs. 1000 and 2000 m,

96   respectively) to maximize the number of profiles spanning each layer yearly.

97   We further use sea surface height (SSH) as a proxy to estimate the OHCA

98   sampling uncertainty in each of the depth intervals mentioned above, building on the

99   work of Lyman and Johnson (2008) for a single 0–700 m layer. This study also builds on

100   that study by making estimates of global OHCA values from in situ data for each layer as

101   outlined above. The earlier study used only proxy data to study sampling uncertainties,

102 without producing actual estimates of OHCA from in situ data. Here we also quantify the

103 effects of infilling on the global integral of OHCA by performing two integrations. One

104 assumes zero anomalies in unsampled regions (the zero-infill mean, or ZIF) and the other

105 that unsampled regions have anomalies equal to the average anomaly of sampled regions

106 (the representative mean, or REP). We also build on previous work, presenting an

107 analysis of how choices of baseline climatology can modify the effects of infilling

108 assumptions on the global OHCA estimates.

109   2.   Data

110 This study uses two sources of data. The Hadley Centre observational dataset EN3_v2a

111 (Ingleby and Huddleston 2007) is used, with XBT and MBT bias corrections of Ishii and

112 Kimoto (2009) applied. All the profiling float data are removed from this dataset, leaving

113 data from temperature profiles from bottle-station reversing thermometers, CTDs, XBTs,

114 MBTs, and moorings. Profiling float data are obtained from the U.S. Argo Global Data

115 Acquisition Center (GDAC), and data from floats with possible pressure drifts are

116 removed (Barker et al. 2011). Delayed-mode data are used when available; otherwise

117 real-time data are used. Only data with quality flags of "good" are retained.

118   We apply additional quality control when computing OHCA to ensure that each

119 layer is adequately sampled. Profiles that do not extend to the bottom depth of a given

120 layer are not considered for that layer. Furthermore, for data from a profile to be used in

121 any given layer, its mean vertical measurement spacing must, on average, be closer than

122 twice the spacing of NODC World Ocean Atlas standard levels from 0 to 100 m, and

123 closer than 3 times the standard level spacing below 100 m.

3.   Method

124

125   OHCA and its sampling uncertainty are computed following Lyman and Johnson (2008),

126   except this time, the OHCA is computed from in situ data instead of proxy data. Aside

127   from the quality control steps mentioned above and the use of in situ data, the other major

128   differences are that OHCA is referenced to a seasonally varying monthly Argo

129   climatology and both the OHCA and its sampling uncertainty are computed for five

130   distinct depth layers (0–100, 100–300, 300–700, 700–900, and 900–1800 m) as detailed

131   below. We discuss curves of the global integral of OHCA for 0–100, 0–300, 0–700, 0–

132   900, and 0–1800 m layers. We compute these curves by adding the global integrals of

133   OHCA for the appropriate sets of mapped layers.

134   *a. OHCA mapping*

135   Heat content in each of the five distinct layers is computed first for every profile. A new

136   seasonal climatology of heat content with monthly resolution is computed using Argo

137   data from 2005 to 2010. This climatology is removed from the heat content profiles to

138   generate anomalies for each layer adequately sampled by the profiles. The results are then

139   objectively mapped using a covariance function with both a large (~1000 km) scale and a

140   small (~100 km) scale (Willis et al. 2004; Lyman and Johnson 2008), assuming a noise-

141   to-signal variance ratio of 2.2. The mapping scales and noise-to-signal ratios could be

142   refined to vary geographically in the future. Ocean temperature covariance scales vary

143   with latitude, becoming elongated in the zonal direction near the equator (e.g., Roemmich

144   and Gilson 2009). They may also vary with depth (e.g., Carton et al. 1996).

145   *b. Global integral of OHCA*

146   We examine two simple assumptions that can be made when computing a global integral

147   of OHCA, again following Lyman and Johnson (2008). The first assumption is that

148   anomalies are zero in regions that are not sampled, a common one for objective mapping.

149   Integrals of the OHCA objective maps using this assumption have been referred to

150   previously as simple integrals or means of the maps (Lyman and Johnson 2008). Here we

151   will use the more descriptive term ZIF. This sort of assumption is commonly used when

152   integrating objective maps (e.g., Ishii and Kimoto, 2009; Levitus et al. 2012), and

153   sometimes when summing bin-averaged data over the globe (Gouretski et al. 2012).

154   The second assumption is that the anomalies in regions that are not sampled are

155   the average of anomalies in sampled regions, an assumption that has also been applied to

156   global sums of bin-averaged data (Palmer et al. 2007). Integrals of OHCA maps using

157   this assumption have been referred to as the weighted integral (Lyman and Johnson

158   2008). Here we will use the term REP. Since objective maps also tend to relax back to

159   zero in areas that are undersampled, making a representative mean using an objective

160   map is slightly more involved than doing so using bin-averaged data. We apply the

161   formalism of Lyman and Johnson (2008) to counteract the tendency of objective maps to

162   relax to zero in data-poor regions when making a representative mean for an objective

163   map. There are other methods for infilling gaps using satellite altimetry data either in an

164   objective mapping formalism (e.g., Willis et al. 2004) or with reduced-space optimal

165   interpolation (e.g., Domingues et al. 2008), but we do not address them here.

166 *c. Sampling uncertainty of global OHCA integrals*

167 Sampling uncertainties are computed in each mapped layer by using Aviso SSH as a

168 proxy for OHCA (Lyman and Johnson 2008). Distinct spatially varying correlation

169 coefficients are computed between SSH and the OHCA content for each mapped layer.

170 The correlation coefficients are larger in the upper 0–100 m and decrease with depth,

171 likely owing to decreasing vertical temperature stratification and eddy energy with depth.

172   When spatially integrating the SSH proxy of OHCA, areas that were not sampled

173 are assumed to have the same anomalies as the area average anomaly of sampled regions.

174 This representative mean yields an unbiased estimate of the global integral of Aviso SSH,

175 bolstering confidence in the sampling uncertainties obtained by the method (Lyman and

176 Johnson 2008). SSH as a proxy for OHCA is most applicable in the upper layers, because

177 SSH variability is dominated by the energetic temperature variability in the strongly

178 stratified upper layers.

179   When adding sampling uncertainties of the distinct depth layers, uncertainties are

180 assumed correlated in areas where both layers are sampled and assumed uncorrelated if

181 sampling areas in different layers do not overlap (Appendix A). These results are

182 dependent on the spatial and temporal scales used in the mapping, as well as the ratio of

183 the unresolved noise and signal variances.

184   While increasing length or time scales for covariance functions increases the

185 amount of data used, the ratio of noise to signal variance could increase as well, so the

186 uncertainty might not decrease. However, lengthening the temporal scale beyond annual

187 cannot overcome aliasing of El Niño or other energetic modes of interannual ocean

188 temperature variability.

189   The sampling uncertainty for the REP is also a measure of how well that method

190   fills in data gaps. The sampling uncertainty is computed by comparing sub-sampled

191   OHCA SSH proxy curves with complete OHCA SSH proxy curves (Lyman and Johnson

192   2008). The complete SSH fields contain eddies, gyres, and some portion of the net

193   warming signal in areas where there are no in situ data. The sampling uncertainty is a

194   measure of how well the infilling represents missing variability that is contained in the

195   complete SSH fields. The REP estimates produce a smaller sampling uncertainty than the

196   ZIF estimates because the former methodology incorporates a better assumption about

197   the contribution of unsampled regions than the latter (Lyman and Johnson 2008).

198   *d. Climatology baseline shifts*

199   We use a climatology based on Argo data from 2005 to 2010 (ClimArgo) because of

200   Argo's even sampling throughout the year and its near-global spatial coverage of the

201   upper 2000 m of the world's oceans. The resulting climatology is a modern one, and thus

202   almost certainly warmer than a long-term mean over our analysis period or conditions in,

203   say, 1950 (as far back in time as estimates are attempted here). Given the sparse

204   sampling, how would the global integrals change if a different, colder climatology were

205   used?

206   We investigate this question by introducing a second climatology, which is just

207   the Argo climatology with values shifted uniformly by a global representative mean

208   estimate of heat content anomaly for each distinct layer in 1950 (Clim1950). We choose a

209   representative mean from 1950 so that the shift in the climatology spans a large but

210   realistic range ($m^{1950,l}$, B3 evaluated at 1950), perhaps an upper bound for the historical

211   record. This shifted Argo climatology is considerably colder than ClimArgo. The better

212 to compare the resulting OHCA curves, the REP global average heat content anomaly

213 from 1950 ($m^{1950,l}A$, B2 evaluated at 1950) is added back to the OHCA curves estimated

214 using Clim1950. This addition shifts the REP curves estimated using Clim1950 to

215 overlay the ClimArgo curves (B11). However, shifts in the ZIF curves estimated using

216 Clim1950 are dependent on the sampling in each year (B10) and do not overlay each

217 other.

4.   Historical sampling

219 The historical record of vertical and horizontal structure of ocean temperature sampling is

220 linked to the history of instrument development. The first worldwide survey of upper

221 ocean temperatures, completed with min-max thermometers, was taken during the

222 Challenger Expedition in 1872–1876. Those data have recently been compared to Argo

223 float data from 2004–2010, finding statistically significant ocean warming over the

224 intervening time interval (Roemmich et al. 2012). The development of the reversing

225 thermometer in 1874 allowed measurement of temperature and depth over full ocean

226 depths to a maximum accuracy of about 0.01ºC and 0.5%, respectively (Warren 2008).

227 However, reversing thermometers require a ship to stop, and historical measurements

228 prior to the International Geophysical Year (1957–1958) are globally very sparse (Boyer

229 et al. 2009).

230   The development of the MBT circa 1938 allowed measurements from a moving

231 ship, although the ship had to slow to a few knots underway for best results, profiles were

232 no deeper than 300 m, often only to 100 m or so, and temperature accuracy was probably

233 not as good as the stated 0.1ºC (Emery and Thomson 1998). MBT depth accuracy is at

234   best 1% (Gouretski and Reseghetti 2010). Nonetheless, MBT profiles are the

235   predominant upper ocean temperature observations from circa 1950 to 1969 (e.g.,

236   Johnson and Wijffels 2011). Their extensive use in the Northern Hemisphere in the

237   Pacific and Atlantic oceans during that time period is evident in the average yearly 0–100

238   m layer sampling density (Fig. 1a). Bottle measurements that extend to depths of 1800 m

239   in these same regions are far less extensive from 1950 to 1969 (Fig. 1e; i; m). The annual

240   sampling fraction, f_l^y, (A2) of the 0–100 m layer exceeds 50% starting in 1956 (Fig. 2).

241   The widespread use of the MBT allows that 50% sampling benchmark to be reached at

242   this early date, but only for the uppermost, 0–100 m, layer.

243   From circa 1970 to 1989, shallow XBTs, profiling as deep as 460 m, are

244   predominant contributors to the historical temperature record (e.g., Boyer et al. 2009;

245   Johnson and Wijffels 2011). Accuracies of ± 0.1°C and ± 2% for temperature and depth,

246   respectively, are specified for the XBT. However, systematic, time-dependent biases can

247   approach or exceed these values (e.g., Gouretski and Reseghetti 2010). The use of the

248   shallow XBT coincides with well-measured temperature (on an annual basis) in the

249   northern hemispheres of all three oceans (now including the Indian Ocean) and extending

250   to the 100–300 m layer (Fig. 1b; f). The Southern Hemisphere subtropics are also

251   somewhat better, although still inadequately (in terms of annual averages) measured in

252   these layers during this time. Reversing thermometer and CTD data collected during this

253   period increase temperature sampling in the 300–700, 700–900, and 900–1800 m layers

254   (Fig. 1l; n). The annual sampling fraction of the 100–300-m layer exceeds 50% starting in

255   1967 (Fig. 2), as a result of the commencement of widespread use of the shallow XBT

256   starting around that time.

257   Deeper XBTs (measuring frequently to at least 700 m, with measurement

258   accuracies and biases similar to the shallow XBTs; e.g., Gouretski and Reseghetti 2010),

259   while introduced earlier, become an important source of historical temperature data from

260   circa 1990 to 2004 (e.g., Johnson and Wijffels 2011) during and after the World Ocean

261   Circulation Experiment (WOCE). During this time period, adequate sampling extends

262   into the Southern Hemisphere subtropics of all three oceans, even to the 300–700 m layer

263   (Fig. 1c; g; k). The annual sampling fraction of the 300–700 m layer exceeds 50%

264   starting in 1983 (Fig. 2) as a result of the increasingly widespread use of the deep XBT

265   during the pre-WOCE large-scale measurement programs. This sampling coverage to 700

266   m peaks at a local temporal maximum of around 79% in 1994 and then declines to a local

267   temporal maximum of 63% in 2001, partly because some XBT data are slow to filter into

268   the data archival centers, and partly as a result of difficulties sustaining gains in ocean

269   observations at the end of WOCE. Deep CTD stations occupied during WOCE further

270   improve sampling in the 700–900 and 900–1800 m (Fig. 1o) layers (but still not

271   adequately outside of the North Atlantic and western North Pacific oceans). These layers

272   also show a similar decline between 1993 and 2000 with the end of WOCE (Fig. 2).

273   The Argo program of autonomous profiling CTD floats (Roemmich et al. 2009)

274   began sampling the upper half of the ocean (nominally to 2000 m) in the year 2000.

275   These floats have nominal temperature accuracy of 0.02ºC, but usually much better and

276   nominal pressure (hence depth) accuracy of 0.12%. By 2005 (and through 2010 and

277   beyond) Argo achieved near-global coverage in the ice-free oceans excluding marginal

278   seas down to 900 m (Fig. 1j). However, the very light surface waters of the tropics

279   presented a challenge for some early Argo floats, and not all of them could profile there

280   much beyond 1000 m, leaving that area slightly undersampled during 2005–2010 (Fig.

281   1p). As more capable floats that can profile from the surface to 2000 m even in the

282   tropics replace the earlier, more limited floats, that coverage gap is gradually being filled.

283   The annual sampling fraction of the 700–900 m layer exceeds 50% starting in 2003 (Fig.

284   2). That same milestone is reached for the 900–1800 m layer starting in 2004 as a result

285   of the increasingly capable and widespread Argo array. By 2010, over 80% of the global

286   ice-free oceans are sampled even to the 900–1800 m layer (Fig. 2).

287   Sampling of the ocean temperature below 2000 m (not treated here) is still very

288   sparse, limited at present to shipboard CTDs. In most areas, comparisons of co-located

289   oceanographic sections (e.g., Purkey and Johnson 2010) or data assimilation into models

290   (e.g., Kouketsu et al. 2011) may be the most appropriate way to assess decadal changes

291   below 2000 m, although it is possible to map multi-decadal changes in ocean heat content

292   in the North Atlantic (e.g., Lozier et al. 2008; Mauritzen et al. 2012), historically the best-

293   sampled ocean.

294   5.   Climatologies and time-varying spatial coverage

295   The method used to globally integrate annual OHCA maps has a large impact on

296   estimates of heat uptake since 1950 in the upper 0–1800 m of the global oceans. The ZIF

297   estimates referenced to ClimArgo (Fig. 3, dashed grey lines) yield a smaller overall rate

298   of heat uptake since 1950 than the REP estimates (Fig. 3, solid black lines) in all depth

299   ranges considered. The ZIF estimates referenced to ClimArgo (presumably warm)

300   climatology tend to relax back to zero when the data coverage for the integrated layers

301   (Fig. 2) becomes sparse. This result occurs because the objective maps relax back to zero

302   anomaly where data are sparse; zero anomaly in most locations will, presumably, tend to

303   be on the warm side of the (poorly known) long-term average because the Argo

304   climatology used is modern (2005–2010). In other words, the annual ZIF estimates using

305   a modern climatology are pulled toward cooler values earlier in time by cooler

306   temperature data, but for times when data are sparse, they relax back to the mean, which

307   is warm owing to the modern climatology used.

308   One way to demonstrate this effect is to use a cooler climatology, Clim1950, to

309   produce contrasting curves for the ZIF estimates (Fig. 3, black dashed lines). Clim1950 is

310   simply a shift of the Argo climatology to the colder mean 1950 values estimated using

311   the representative mean anomalies for each layer. It is about the coldest reasonable

312   climatology that could be used for assessing heat content changes over this time period.

313   The use of Clim1950 results in a much larger warming trend for the curves produced

314   from ZIF estimates than does the use of ClimArgo. This difference arises solely because

315   ZIF estimates assume zero anomalies in unsampled regions. With a climatology shifted to

316   colder 1950 mean values, the large extents of the maps with sparse data in the early years

317   all relax back to relatively colder 1950 mean values as a baseline, rather than the warmer

318   Argo climatology values. In the more recent years, the larger sampled fraction of the

319   global ocean (Fig. 2) means that ZIF estimates for either the colder Clim1950 or the

320   warmer modern ClimArgo are more constrained by data to be similar (Fig. 3). Hence, for

321   the ZIF estimates, the changing and sometimes sparse sampling patterns combine with

322   the climatology to produce trends that depend on the climatology values, especially if

323   those trend estimates span times of sparse sampling. Shifting the Argo climatology using

324   representative means between 1950 and 2000 produce similar shifts in the ZIF estimates

325   (B10, plots not shown).

326   The size of the shifts in the ZIF estimates is dependent on the fraction of the globe

327   that is covered each year by in situ sampling and by the magnitude of the mean shift (B7).

328   The result may not always be intuitive. For example, in 2010, the 0–1800 m Clim1950

329   ZIF value is 50 ZJ less than the ClimArgo ZIF value (Fig. 3, panel d, dashed lines),

330   despite Argo's near global coverage in 2010. We can compute the expected size of the

331   shift from B10: The mean shift that the Clim1950 curve experiences in 2010 is

332   $(1 - f_{0-1800}^{2010})m^{1950,0-1800}A$. In this case, $m^{1950,0-1800}A \approx -500\ ZJ$ (Fig. 3, panel d) and

333   $f_{0-1800}^{2010} \approx .9$ (Fig. 2), so the observed offset in 2010 of 50 ZJ is to be expected. An

334   intermediate climatology, say one shifted to 1980 levels, would result in a smaller cold

335   bias in modern times, but a large warm bias in earlier times.

336   Unlike the ZIF estimates, the REP estimates (Fig. 3, black solid line) are the same

337   for both the Clim1950 values and the ClimArgo (B11). This result holds because the REP

338   estimates avoid any relaxation back to climatological values by assuming that the mean

339   anomaly of the sampled regions applies to the unsampled regions.

340   ## 6.   Sampling uncertainty

341   Computing the global integral using the REP estimates increases both the signal within

342   and the noise from the observed areas of the global ocean by extending them to the

343   unmeasured areas (Lyman and Johnson 2008). The sampling uncertainty (Fig. 4), which

344   generally grows as sampling becomes sparse (Fig. 2), is only one component of the total

345   uncertainty (e.g., Lyman et al. 2010). Here we do not concern ourselves with other

346   contributions, but there is much work being done by the international scientific

347 community on quantifying uncertainties remaining in XBT and MBT bias corrections, as

348 well as those owing to differences in quality control, mapping, and climatology.

349   Sampling uncertainty (Fig. 4) increases greatly with decreased area coverage (Fig.

350 2), so it ramps up going back in time prior to about 1956 in the 0–100 m layer. After that

351 date, around the time of the International Geophysical Year (IGY), MBT use expanded.

352 The advent of the IGY further reduces sampling uncertainties in all layers because of a

353 rise in reversing thermometer data from deep oceanographic stations. The sampling

354 uncertainty for 0–300 m declines further after around 1969, with the increasingly

355 widespread use of the shallow XBT, and decreases markedly for 0–700 m around 1990,

356 with the more widespread use of the deep XBT and the advent of WOCE. Again, WOCE

357 reduces sampling uncertainty in all layers during the 1990s because of increased CTD

358 stations worldwide. However, around the year 2000, there is a slight increase in sampling

359 uncertainty in all layers as WOCE sampling winds down before Argo sampling spins up.

360 Starting around 2001–2003, sampling uncertainties in all layers begin to shrink, reaching

361 a historical low by 2005–2006, depending on the depth of integration, and remaining

362 small as Argo coverage continues to improve.

363   Sampling uncertainties (Fig. 4) generally decrease as areal coverage (Fig. 2)

364 increases. This inverse relationship is not perfect, at least partly because OHCA variance

365 is spatially variable, so increasing sampling in one region might reduce sampling

366 uncertainty more than increasing it the same amount in another region. Furthermore, the

367 contribution to sampling uncertainty in deeper layers is relatively small even though the

368 area sampled is also small, except in recent years. This situation likely holds owing to the

369 decreasing heat content anomaly signals of eddies, planetary waves, gyre shifts, and even

370 the net warming signal with increasing depth.

371   7.   Discussion

372 Ocean warming is observed between 1950 and 2011 in all layers for both methods of

373 global integration: zero-infilled (ZIF) or representative (REP) means (Fig. 3). However,

374 the REP estimates are more likely to result in an unbiased trend (Lyman and Johnson

375 2008). Furthermore, we show that the REP estimates are insensitive to mean shifts in the

376 background climatology, whereas the trends from the ZIF estimates vary greatly

377 depending on such shifts. For a modern (warmer) climatology, ZIF estimates for early,

378 poorly sampled years shift back toward zero anomaly (warm conditions), increasingly

379 reducing the warming trend the further back in time that trend is computed. In contrast,

380 for climatologies shifted to early (colder) values, ZIF estimates for early years are cold,

381 but more appropriately warm in later years because the data coverage of the warmed

382 oceans is improved in recent years. This difference results in a very different trend

383 depending on the climatology for ZIF estimates. While further analyses are needed to

384 quantify the impacts of regional variability in climatologies (rather than the global shifts

385 applied here) on the OHCA curves, REP estimates provide an estimate of the warming

386 rate that does not depend on the mean heat content of the climatology and are preferable

387 to ZIF estimates.

388   Here we only compute and analyze sampling uncertainties. Before the

389 significance of the trends in the global integral OHCA can be completely determined

390 over various lengths of the historical record, it will be necessary to examine other sources

391 of uncertainty in more detail. These include uncertainties owing to quality control, choice

392   of XBT and MBT bias correction, choice of climatology, and choice of mapping method.

393   Nonetheless, when areal coverage gets smaller, OHCA sampling uncertainties generally

394   get larger. There is a roughly inverse relationship between these quantities in each layer,

395   with smaller and smaller contributions of the uncertainty per unit depth with increasing

396   depth (not shown). Of course, the warming signal in the upper 1800 m also gets smaller

397   per unit depth with increasing depth (e.g., Johnson and Wijffels 2011). The 50%

398   coverage benchmark (Fig. 3, vertical lines) discussed above for the different layers is

399   arbitrary, but a reminder that below some areal coverage, it becomes difficult to make a

400   realistic estimate of the global integral OHCA for a given year in a given layer, no matter

401   the mapping method.

402   In Lyman and Johnson (2008), a similarly arbitrary benchmark of 10 ZJ was used

403   to highlight that sampling before 1967 produced large uncertainties. That benchmark

404   roughly corresponded to the 50% coverage level benchmark used here (Fig. 1, Lyman

405   and Johnson 2008). In Lyman and Johnson (2008), shallow XBTs were extended to 700

406   m following Willis et al. (2004), but that extrapolation technique is not employed here.

407   As a result, before widespread use of the deep XBT, the 0–700 m sampling density in

408   Lyman and Johnson (2008) roughly corresponds to the 100–300 m sampling density here,

409   which reaches 50% in 1967. The 300–700 m sampling density here does not reach 50%

410   until 1983, when the deep XBT came into widespread use.

411   Computation of the sampling uncertainty requires the assumption that SSH is

412   directly proportional to OHCA in a depth layer. While this is a reasonable assumption,

413   the two are not directly related because SSH also depends on OHCA over the entire water

414   column, changes in salinity, and mass changes. On the other hand, sampling density is a

415 product of the mapping and requires no assumption about the relationship of SSH to

416 OHCA. Finally, it would seem unwise to apply infilling assumptions to over 50% of the

417 mapping area when computing a global integral; thus, the 50% benchmark is a reasonable

418 choice.

419   We estimate warming rates for the different layers by computing trends using

420 unweighted least squares REP OHCA annual values from the benchmark years of 1956,

421 1967, 1983, and 2004, through the final year, 2011 (Table 1). We do not use a weighted

422 least squares formalism or report uncertainties because the sampling uncertainties

423 estimated here are not the full uncertainty, which can be much larger (Lyman et al. 2010).

424 For adequately sampled time periods, warming trends generally increase with increasing

425 depth, as the surface-intensified warming signal penetrates to at least 1500 m (e.g.,

426 Levitus et al. 2012). In recent years, from 2004 to 2011, while the upper ocean is not

427 warming, the ocean continues to absorb heat at depth (e.g., Levitus et al. 2012; von

428 Schuckman and Le Traon 2011), here estimated at a rate of 0.56 W m^{-2} when integrating

429 over 0–1800 m. The warming estimated here for 0–700 m from 1993 through 2011 is

430 0.56 W m^{-2}, whereas that for our previously published curve is 0.48 W m^{-2} (Johnson et al.

431 2012). The historical rates for 0–100, 0–300, and 0–700 m estimated here are generally

432 larger than other analyses (e.g., Levitus et al. 2012; Ishii and Kimoto 2009; Domingues et

433 al. 2008), at least partly owing to our use of REP, which increases the trend by assuming

434 the anomaly in unsampled areas is the same as the mean anomaly of sampled areas.

435   Finally, while XBT biases have received much attention in the last few years,

436 MBTs are a large source of upper ocean temperature data from the 1950s through the

437 1960s, and their biases have been estimated by only a few investigators (e.g., Gouretski

438 and Reseghetti 2010; Ishii and Kimoto, 2009). Sampling uncertainties for the REP

439 estimate during this early time period are large (Fig. 4); however, the warming signal is

440 also large (Fig. 3). In order to determine if this large signal is statistically significant, it

441 will be necessary to estimate all possible sources of uncertainty, including uncertainties

442 in MBT bias corrections.

454

APPENDIX A. Summation of Uncertainty

455

456   *Sampling uncertainty computation*

457   In using Aviso SSH as a proxy for every depth layer of OHCA (following Lyman and

458   Johnson 2008), we implicitly assume that eddy statistics of the upper layers are similar to

459   deep layers. In each depth layer the local correlations of Aviso SSH with OHCA are

460   estimated on a coarse grid. The resulting coefficients are used to construct proxy OHCA

461   fields that are then subsampled in locations of in situ observation. Sampling uncertainty

462   in a depth layer (SE_j, where the integer numbers 1, 2, 3, 4, and 5 have been assigned the

463   0–100, 100–300, 300–700, 700–900, and 900–1800-m layers, respectively), is defined as

464   the standard deviations of the differences between heat content curves computed from the

465   proxy OHCA fields and the in situ OHCA fields (Lyman and Johnson 2008).

466   *Addition of sampling uncertainty when summing depth layer OHCA*

467   We also make another assumption, that the correlated sampling uncertainty in depth layer

468   j between depth layers i and j ($CorrSE_{ij}$) is proportional to the square root of the

469   percentage change in the globe coverage for depth layer i ($\dfrac{\Delta_i^y}{f_j^y}$):

$$CorrSE_{ij} \equiv \begin{array}{l} SE_j \sqrt{\dfrac{\Delta_i^y}{f_j^y}}, \ i \geq j \\ 0, \ i < j \end{array}, \qquad (A1)$$

471

472   where $\Delta_l^y \equiv f_l^y - f_{l-1}^y$. Note that $\Delta_5^y = f_5^y$, because layer 5 is the bottom layer and

473    $\displaystyle\sum_{l=1}^{5} \Delta_l^y = f_1^y.$

474   The fractional coverage (f_l^y) for depth layer l and year y is defined as

475
$$f_l^y = \frac{\displaystyle\sum_{\substack{i=0,I \\ j=0,J}} \langle 1_k \rangle_{i,j} \, dA_{i,j}}{A}, \tag{A2}$$

476   where $\langle 1_k \rangle_{i,j}$ is the sampling density for a given data distribution, obs_k. The sampling

477   density is a linear mapping to location i, j where each datum at position k, for depth

478   layer l and year y, has been replaced by unity. Here $dA_{i,j}$ is the area represented by the

479   location i, j, and $A \equiv \displaystyle\sum_{\substack{i=0,I \\ j=0,J}} dA_{i,j}$, the total area mapped (taken from Lyman and Johnson

480   2008). Also, f_l^y and $\langle 1_k \rangle_{i,j}$ quantify the density of the sampling based on the data

481   distribution, the temporal and spatial scales of the mapping, and the noise-to-signal

482   variance ratio of the mapping (Lyman and Johnson 2008). This methodology is a more

483   quantitative assessment of sampling density than other methods sometimes used, such as

484   summing the area of boxes that contain more than some arbitrary threshold of data points.

485   Summing the correlated sampling uncertainties from the surface to the bottom of

486   a given depth layer and then adding the resulting uncertainties in quadrature (thus

487   assuming they are uncorrelated) yields:

488
$$TSE_m = \sqrt{\sum_{i=1}^{5}\left[\sum_{j=1}^{m} CorrSE_{ij}\right]^2}, \tag{A3}$$

489   where TSE_m is the total sampling uncertainty from the surface to the bottom of layer m.

490

APPENDIX B. Global Integrals

490

491   *Effects of climatology baseline shifts on global integrals*

492   Two global integrals are examined in this paper, one based on the zero-infilled integrals

493   or means (*ZIF*) and the other based on the representative integrals or means (*REP*). They

494   can be defined as

495
$$ZIF = \sum_{\substack{i=0,I \\ j=0,J}} \left\langle obs_k \right\rangle_{i,j} dA_{i,j} \tag{B1}$$

496   and

497
$$REP = \frac{A \displaystyle\sum_{\substack{i=0,I \\ j=0,J}} \left\langle obs_k \right\rangle_{i,j} dA_{i,j}}{\displaystyle\sum_{\substack{i=0,I \\ j=0,J}} \left\langle 1_k \right\rangle_{i,j} dA_{i,j}}, \tag{B2}$$

498   where $\left\langle obs_k \right\rangle_{i,j}$ is a linear mapping of some distribution of observation (obs_k) on a depth

499   layer l and for year y to a location i, j and the other terms are defined in Appendix A.

500   If the obs_k on depth layer l are shifted by a constant value, in this case the

501   representative mean for year $ym,$ then

502
$$\left(m_k^{ym,l} \equiv \frac{\displaystyle\sum_{\substack{i=0,I \\ j=0,J}} \left\langle obs_k \right\rangle_{i,j} dA_{i,j}}{\displaystyle\sum_{\substack{i=0,I \\ j=0,J}} \left\langle 1_k \right\rangle_{i,j} dA_{i,j}} \right). \tag{B3}$$

503   Here the mapping $\left\langle obs_k \right\rangle_{i,j}$ is dependent on year, $ym,$ and depth layer, $l.$ Adding this shift

504   B1 and B2 become

505
$$ZIF^s = \sum_{\substack{i=0,I \\ j=0,J}} \left\langle obs_k - m_k^{ym,l} \right\rangle_{i,j} dA_{i,j} \tag{B4}$$

506   and

$$REP^s = \frac{A \sum_{\substack{i=0,I \\ j=0,J}} \left\langle obs_k - m_k^{ym,l} \right\rangle_{i,j} dA_{i,j}}{\sum_{\substack{i=0,I \\ j=0,J}} \left\langle 1_k \right\rangle_{i,j} dA_{i,j}},$$ (B5)

507

508   where ZIF^s and REP^s are integrals that have been shifted by this spatially uniform

509   mean. Since the mappings are linear and $m_k^{ym,l}$ is spatially constant, therefore not

510   dependent on k, B4 and B5 become

511

512    $$ZIF^s = \sum_{\substack{i=0,I \\ j=0,J}} \left\langle obs_k \right\rangle_{i,j} dA_{i,j} - m^{ym,l} \sum_{\substack{i=0,I \\ j=0,J}} \left\langle 1_k \right\rangle_{i,j} dA_{i,j}$$ (B6)

513   and

514    $$REP^s = \frac{A \sum_{\substack{i=0,I \\ j=0,J}} \left\langle obs_k \right\rangle_{i,j} dA_{i,j}}{\sum_{\substack{i=0,I \\ j=0,J}} \left\langle 1_k \right\rangle_{i,j} dA_{i,j}} - \frac{A m^{ym,l} \sum_{\substack{i=0,I \\ j=0,J}} \left\langle 1_k \right\rangle_{i,j} dA_{i,j}}{\sum_{\substack{i=0,I \\ j=0,J}} \left\langle 1_k \right\rangle_{i,j} dA_{i,j}}.$$ (B7)

515   Eq. B6 and B7 simplify to

516    $$ZIF^s = ZIF - f_l^y m^{ym,l} A$$ (B7)

517   and

518    $$REP^s = REP - m^{ym,l} A,$$ (B9)

519   where f_l^y is the fractional coverage (A2). Thus REP^s has shifted by area integral of

520   representative mean for year ym, $m^{ym,l} A$ (B2 evaluated at ym). This shift is independent

521   of the sampling in the mapping and therefore independent of the year that of the map, y.

522   On the other hand, ZIF^s is shifted by the fraction of the area integral of representative

523   mean that was sampled, $f_l^y m^{ym,l} A$, and is dependent on y. These results are independent

524   of mapping or mean offset.

525   When plotting shifted OHCA curves, it is useful to offset the results in order to

526   focus attention on changes in trends rather than simple offsets. Here we have chosen to

527   offset the shifted OHCA curves by the area integral of the climatology offset, $m^{ym,l} A$. For

528   plotting purposes, B7 and B9 now become:

529    $$ZIF^s = ZIF + m^{ym,l} A\left(1 - f_l^y\right)$$ (B10)

530   and

531    $$REP^s = REP.$$ (B11)

532   Thus, the REP result is independent of baseline shifts in climatology, whereas the ZIF

533   result for any given year is sensitive to baseline shifts proportional to the unsampled area

534   for that year.

535 **References**

536 Barker, P. M., J. R. Dunn, C. M. Domingues, and S. E. Wijffels, 2011: Pressure sensor

537   drifts in Argo and their impacts. *J. Atmos. Oceanic Technol.*, **28**, 1036–1049,

538   doi:10.1175/2011JTECHO831.1.

539 Bindoff, N. L., and Coauthors, 2007: Observations: Oceanic climate change and sea

540   level. *Climate Change 2007: The Physical Science Basis*, S. Solomon et al., Eds.,

541   Cambridge University Press, 385–432.

542 Boyer, T. P., and Coauthors, 2009: *World Ocean Database 2009.* S. Levitus, Ed., NOAA

543   Atlas NESDIS 66, U.S. Gov. Printing Office, Wash., D.C., 216 pp., DVDs.

544 Carton, J. A., B. S. Giese, X. Cao, and L. Miller, 1996: Impact of altimeter, thermistor,

545   and expendable bathythermograph data on retrospective analyses of the tropical

546   Pacific Ocean. *J. Geophys. Res.*, **101**, 14 147–14 159, doi:10.1029/96JC00631.

547 Domingues, C. M., J. A. Church, N. J. White, P. J. Gleckler, S. E. Wijffels, P. M. Barker,

548   and J. R. Dunn, 2008: Improved estimates of upper-ocean warming and multi-decadal

549   sea level rise. *Nature*, **453**, 1090–1094, doi:10.1038/nature07080.

550 Emery, W. J., and R. E. Thomson, 1998: *Data Analysis Methods in Physical*

551   *Oceanography*. Elsevier, Oxford, 634 pp.

552 Gouretski, V., and F. Reseghetti, 2010: On depth and temperature biases in

553   bathythermograph data: Development of a new correction scheme based on analysis

554   of a global ocean database. *Deep-Sea Res. I*, **57**, 812–833,

555   doi:10.1016/j.dsr.2010.03.011.

556   Gouretski, V., J. Kennedy, T. Boyer, and A. Köhl, 2012: Consistent near-surface ocean

557   warming since 1900 in two largely independent observing networks. *Geophys. Res.*

558   *Lett.*, **39**, L19606, doi:10.1029/2012GL052975.

559   Ingleby, B., and M. Huddleston, 2007: Quality control of ocean temperature and salinity

560   profiles—historical and real-time data. *J. Mar. Syst.*, **65**, 158–175, doi:

561   10.1016/j.jmarsys.2005.11.019.

562   Ishii, M., and M. Kimoto, 2009: Reevaluation of historical ocean heat content variations

563   with time-varying XBT and MBT depth bias corrections. *J. Oceanogr.*, **65**, 287–299,

564   doi:10.1007/s10872-009-0027-7.

565   Johnson, G. C., J. M. Lyman, J. K. Willis, S. Levitus, T. Boyer, J. Antonov, and S. A.

566   Good, 2012: Global Oceans: Ocean Heat Content. In State of the Climate in 2011,

567   Blunden, J., and D. S. Arndt, Eds., *Bulletin of the American Meteorological Society*,

568   **93**, 7, S62-S65, doi:10.1175/2012BAMSStateoftheClimate.1.

569   Johnson, G. C., and S. E. Wijffels, 2011: Ocean density change contributions to sea level

570   rise. *Oceanogr.*, **24(2)**, 112–121, doi:10.5670/oceanog.2011.31.

571   Kouketsu, S., and Coauthors, 2011: Deep ocean heat content changes estimated from

572   observation and reanalysis product and their influence on sea level change. *J.*

573   *Geophys. Res.*, **116**, C03012, doi:10.1029/2010JC006464.

574   Levitus, S., J. Antonov, and T. Boyer, 2005: Warming of the World Ocean, 1955–2003.

575   *Geophys. Res. Lett.*, **32,** L02604, doi:10.1029/2004GL021592.

576   Levitus, S., J. I. Antonov, T. P. Boyer, R. A. Locarnini, H. E. Garcia, and A.V.

577   Mishonov, 2009: Global ocean heat content 1955–2008 in light of recently revealed

578   instrumentation problems. *Geophys. Res. Lett.*, **36**, L07608,

579   doi:10.1029/2008GL037155.

580   Levitus, S., and Coauthors, 2012: World ocean heat content and thermosteric sea level

581   change (0–2000 m), 1955–2010. *Geophys. Res. Lett.*, **39**, L10603,

582   doi:10.1029/2012GL051106.

583   Lozier, M. S., S. J. Leadbetter, R. G. Williams, V. Roussenov, M. S. C. Reed, and N. J.

584   Moore, 2008: The spatial pattern and mechanisms of heat content change in the North

585   Atlantic. *Science*, **319**, 800–803.

586   Lyman, J. M., and G. C. Johnson, 2008: Estimating annual global upper ocean heat

587   content anomalies despite irregular in situ ocean sampling. *J. Climate*, **21**, 5629–

588   5641, doi:10.1175/2008JCLI2259.1.

589   Lyman, J. M., S. A. Good, V. V. Gouretski, M. Ishii, G. C. Johnson, M. D. Palmer, D. M.

590   Smith, and J. K. Willis, 2010: Robust warming of the global upper ocean. *Nature*,

591   **465**, 334–337, doi:10.1038/nature09043.

592   Mauritzen, C., A. Melsom, and R. T. Sutton, 2012: Importance of density-compensated

593   temperature change for deep North Atlantic Ocean heat uptake, *Nature Geosci.*, **5**,

594   905–910.

595   Palmer, M. D., and P. Brohan, 2011: Estimating sampling uncertainty in fixed-depth and

596   fixed-isotherm estimates of ocean warming. *Int. J. Climatol.* **31**, 980–986,

597   doi:10.1002/joc.2224.

598   Palmer, M. D., K. Haines, S. F. B. Tett, and T. J. Hansell, 2007: Isolating the signal of

599   ocean global warming. *Geophys. Res. Lett.*, **34**, L23610, doi:

600   10.1029/2007GL031712.

601   Palmer, M. D., and Coauthors, 2010: Future observations for monitoring global ocean

602   heat content, in *Proceedings of the OceanObs' 09: Sustained Ocean Observations and*

603   *Information for Society Conference* (Vol. 2), Venice, Italy, 21–25 September 2009, J.

604   Hall, D. E. Harrison, and D. Stammer, Eds., ESA Publication WPP-306.

605   Purkey, S. G., and G. C. Johnson, 2010: Warming of global abyssal and deep Southern

606   Ocean between the 1990s and the 2000s: Contributions to global heat and sea level

607   rise budgets. *J. Climate*, **23**, 6336–6351, doi:10.1175/2010JCLI3682.1.

608   Roemmich, D., and J. Gilson, 2009: The 2004–2008 mean and annual cycle of

609   temperature, salinity, and steric height in the global ocean from the Argo Program

610   *Prog. Oceanogr.*, **82**, 81–100.

611   Roemmich, D., and Coauthors, 2009: The Argo Program: Observing the global oceans

612   with profiling floats. *Oceanogr.*, **22(2)**, 34–43.

613   Roemmich, D., W. J. Gould, and J. Gilson, 2012: 135 years of global ocean warming

614   between the Challenger expedition and the Argo Programme. *Nature Climate*

615   *Change*, **2**, 425–428, doi:10.1038/nclimate1461.

616   von Schuckmann, K., and P.-Y. Le Traon, 2011: How well can we derive global ocean

617   indicators from Argo data? *Ocean Sci.*, **7**, 783–791, doi:10.5194/os-7-783-2011.

618   von Schuckmann, K., F. Gaillard, and P.-Y. L. Traon, 2009: Global hydrographic

619   variability patterns during 2003–2008. *J. Geophys. Res.*, **114**, C09007,

620   doi:10.1029/2008JC005237.

621   Warren, B. A., 2008: Nansen-bottle stations at the Woods Hole Oceanographic

622   Institution. *Deep-Sea Res. I*, **55**, 379–395, doi: /10.1016/j.dsr.2007.10.003.

623   Willis, J. K., D. Roemmich, and B. Cornuelle, 2004: Interannual variability in upper

624   ocean heat content, temperature, and thermosteric expansion on global scales, *J.*

625   *Geophys. Res.*, **109**, C12036, doi:10.1029/2003JC002260.

626

626 Table 1. Warming reported as heat flux applied to Earth's entire surface area (in W m^{-2})

627 corresponding to trends in annual REP OHCA estimates from unweighted linear fits from

628 benchmark years through 2011 for different depths of integration (left column). A

629 benchmark year is defined as the year in which sampling coverage first exceeds 50%, and

630 remains > 50% thereafter. Layer warming trends over time periods during which

631 coverage in a layer is < 50% in any year are not reported, indicated here by a dash.

	Time Period			
Depth layer	1956–2011	1967–2011	1983–2011	2004–2011
0–100 m	0.06 W m^{-2}	0.08 W m^{-2}	0.08 W m^{-2}	0.01 W m^{-2}
0–300 m	–	0.18 W m^{-2}	0.24 W m^{-2}	0.19 W m^{-2}
0–700 m	–	–	0.46 W m^{-2}	0.30 W m^{-2}
0–1800 m	–	–	–	0.56 W m^{-2}

632

632
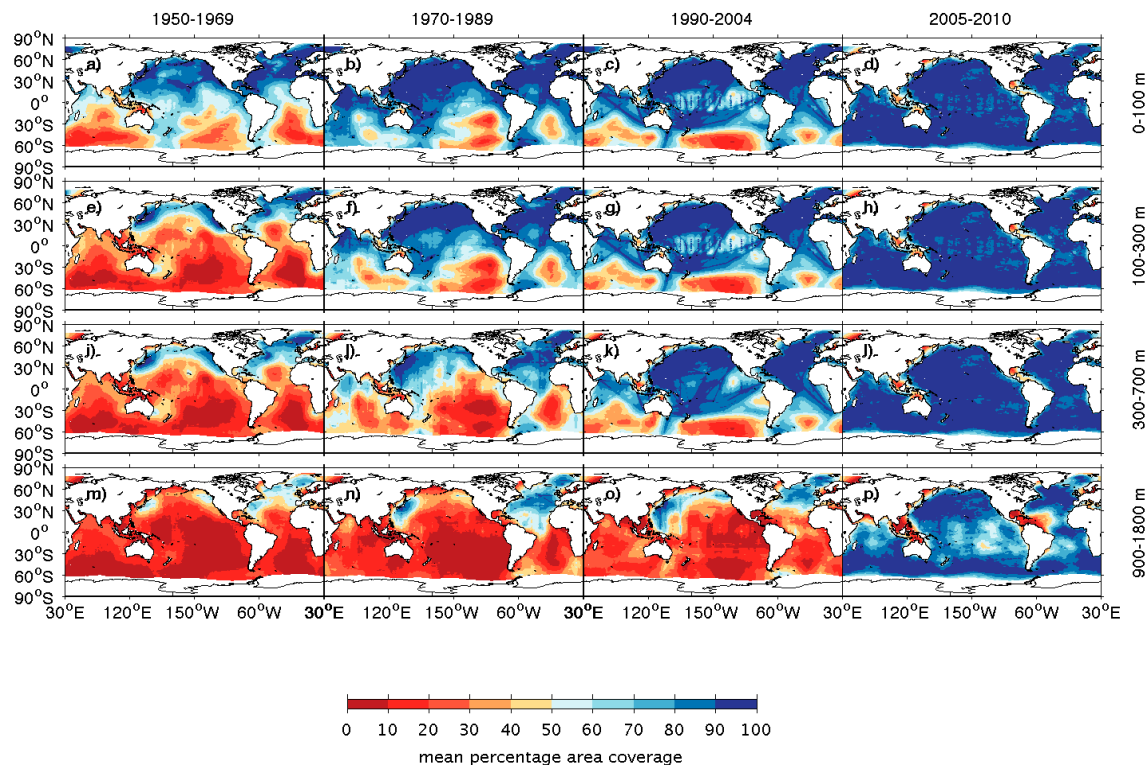
FIG. 1. Means of annual in situ temperature data sampling density (see A3) for various depth layers and time ranges. From top to bottom: 0–100 m, 100–300 m, 300–700 m, and 900–1800 m. From left to right: 1950–1969, 1970–1989, 1990–2004, and 2005–2010.
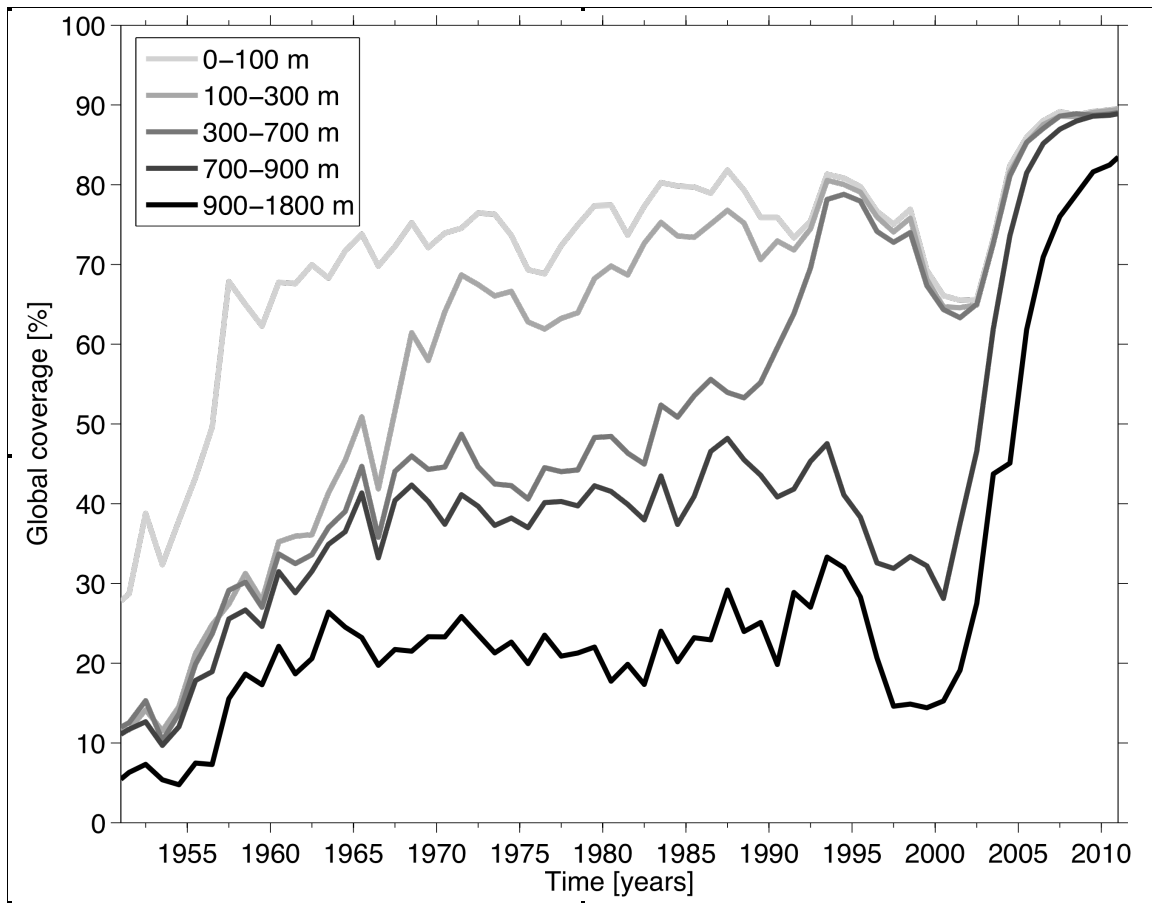
637

638   FIG. 2. Annual fractional coverage of global ice-free ocean sampled for in situ ocean

639   temperature (see A2) for (proceeding from lightest grey to black lines) 0–100 m, 100–300

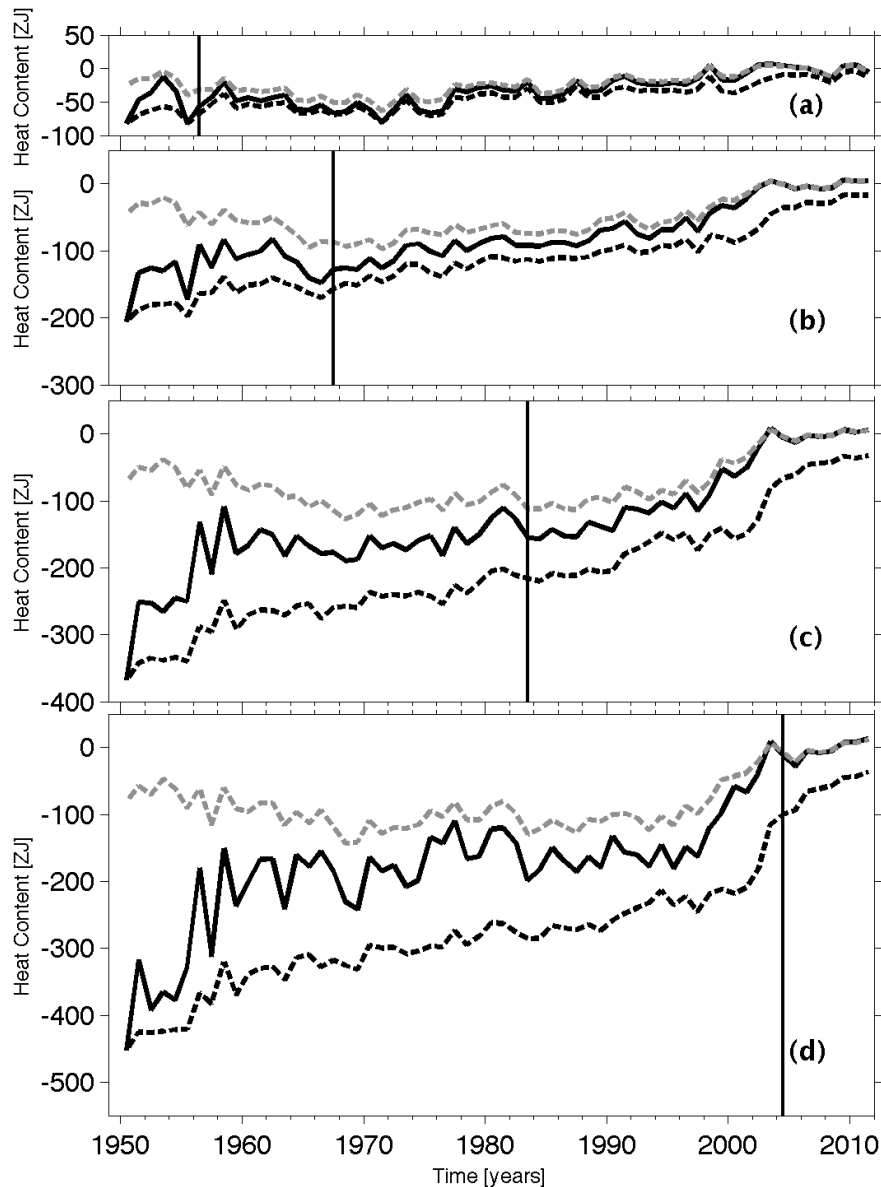640   m, 300–700 m, 700–900 m, and 900–1800 m.

641

FIG. 3. Time series of annual average global integrals of upper ocean heat content

anomaly (10^{21} J, or ZJ) for (a) 0–100 m, (b) 0–300 m, (c) 0–700 m, and (d) 0–1800 m.

Time series are shown using ZIF estimates relative to both ClimArgo (dashed grey lines)

and Clim1950 (dashed black lines). Time series are also shown using REP estimates

(black solid lines), which are not affected by shifts in the mean climatology (B11). Thin

vertical lines denote when the coverage (Fig. 2) reaches 50% for (a) 0–100 m, (b) 100–

300 m, (c) 300–700 m, and (d) 900–1800 m.

649

650
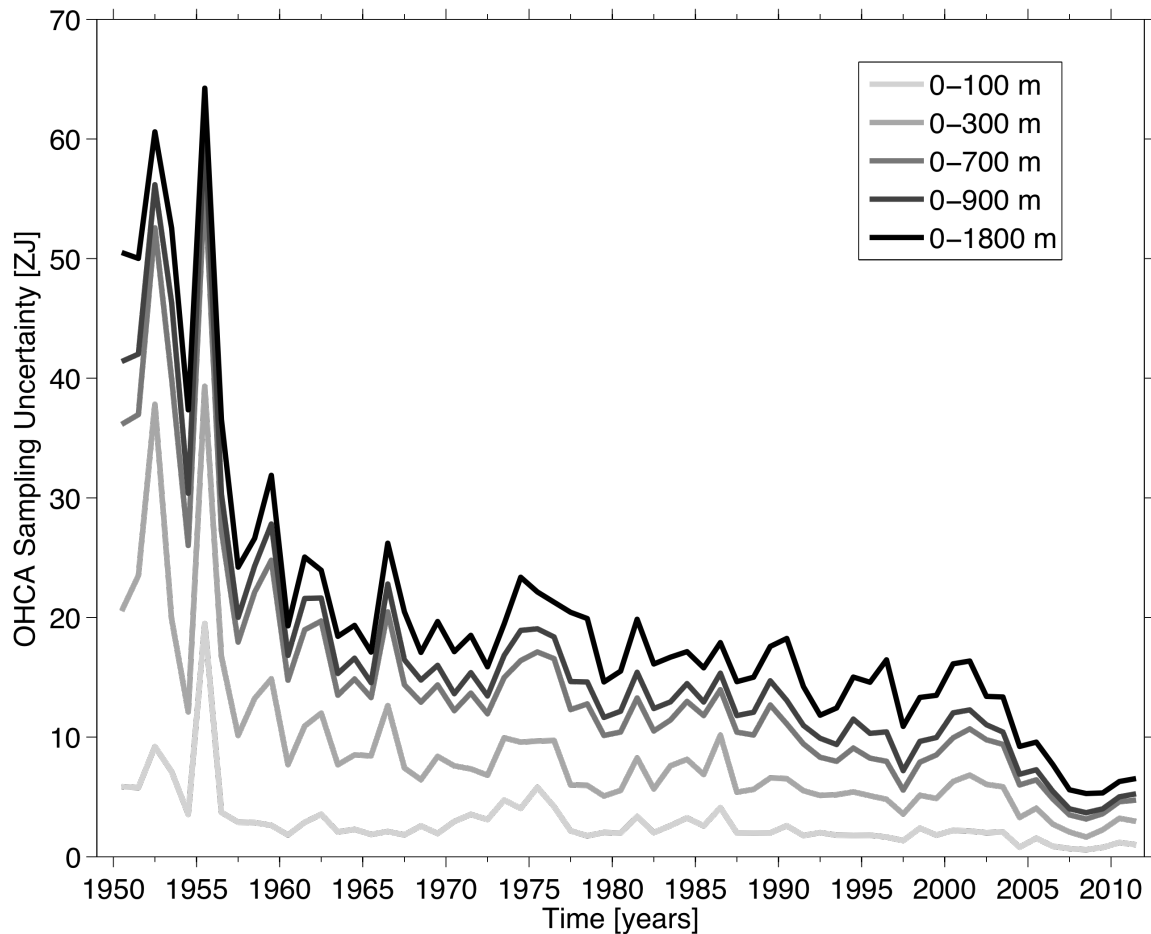
651 Fɪɢ. 4. Estimates of sampling uncertainties for the ZIF estimates (following Lyman and

652 Johnson 2008) at one standard error of the mean for (proceeding from lightest grey to

653 black lines) 0–100 m, 0–300 m, 0–700 m, 0–900 m, and 0–1800 m. Uncertainties are

654 computed by summing up sampling uncertainties for each layer from the surface

655 downwards (Appendix A). Where sampled layers overlap in space, uncertainties are

656 added. Where sampled layers do not spatially overlap, uncertainties are summed in

657 quadrature.